Research Article

Yicheng Deng, Xianyin Leng*, Wei Guan, Zhixia He, Wuqiang Long, Shengli Wei, and Jie Hu

A numerical study on the in-nozzle cavitating flow and near-field atomization of cylindrical, V-type, and Y-type intersecting hole nozzles using the LES-VOF method

https://doi.org/10.1515/gps-2022-0015
received July 25, 2021; accepted December 21, 2021

Abstract: In order to improve the performance of engines fueled with diesel fuel or diesel-like e-fuels so as to realize greener transportation, the V-type and Y-type intersecting hole nozzles, in which each hole is formed by the coalescence of two or three subholes, have been designed. In this article, the multiphase flow inside and outside the nozzle was numerically investigated using a volume-of-fluid large eddy simulation (VOF-LES) method to clarify the effects of the nozzle structure on the cavitating flow and primary atomization characteristics. The calculation was carried out at an injection pressure of 150 MPa and a back pressure of 0.1 MPa. Numerical results showed that unlike the L-shape pressure distribution along a cylindrical hole, for intersecting type hole nozzles, the pressure showed a stepped shape drop along the holes due to the overall convergent hole structure, which restrained the inception of cavitation. Consequently, the global loss of the flow over an intersecting type hole nozzle was lower by 24–37% than those of a cylindrical hole nozzle. Additionally, the jets emerging from the intersecting hole nozzles showed 50% wider spreading angles and 27% smaller droplet sizes than those of the cylindrical hole nozzle. Furthermore, the jets emerging from a Y-type intersecting hole nozzle showed enhanced atomization, which was found to be due to the unstable air suction near the outlets of this type of nozzle hole.

Keywords: diesel nozzle, intersecting hole, internal flow, near field jet, large-eddy simulation

* **Corresponding author: Xianyin Leng,** Institute for Energy Research, Jiangsu University, Zhenjiang 212013, China, e-mail: lxy@ujs.edu.cn
Yicheng Deng, Shengli Wei: School of Automotive and Traffic Engineering, Jiangsu University, Zhenjiang 212013, China
Wei Guan, Zhixia He: Institute for Energy Research, Jiangsu University, Zhenjiang 212013, China
Wuqiang Long: Institute for Internal Combustion Engines, Dalian University of Technology, No. 2 Linggong Road, Dalian, Liaoning 116023, China
Jie Hu: Faculty of Engineering, Kitami Institute of Technology, 165 Koen-cho, Kitamishi, Hokkaido, 090-8507, Japan

1 Introduction

Nowadays, sustainable development has become a general consensus all over the world. In the transportation sector, many researchers are discussing the transition from internal combustion engine vehicles to electric vehicles for green transportation [1,2]. However, for commercial vehicles and heavy-duty non-road machinery, a diesel engine will continue to be used for a long time due to the superior advantages of diesel fuel in energy density [3,4]. On the other hand, in view of the unstableness of electricity generation from some green energy (e.g., wind or solar energy), it has been proposed to produce synthetic fuels using waste biomass and renewable energy as a smart way to store renewable electric energy when a production peak occurs. It is a green chemical process that forms hydrocarbons, denominated as electro-fuel (e-fuel), from H_2 (produced by electrolysis of water) and CO_2 captured from industrial or biosources [5,6]. For the convenience of using the existing engine technologies and fuel charging infrastructures, some of these e-fuels will be designed to have physical and chemical properties similar to diesel fuel [7–9]. In this sense, diesel engines will continue to exist for the long term. Under such background, it is of crucial importance to develop advanced fuel injection and combustion technologies to further improve performances and to reduce harmful emissions of engines fueled with diesel or diesel-like e-fuels [10,11].

To this end, a large number of investigations have focused on how to promote the in-cylinder atomization

and fuel–air mixing processes for diesel engines [12,13]. Generally, it is desired that the spray has a high penetration speed, large spray angle, and fine droplets [14,15]. For several decades, a number of studies have confirmed that increasing the injection pressure was an effective way to promote atomization and mixing of the fuel and air, improving performances of diesel engines [16–18]. However, it seems there is a limit to improving fuel atomization by increasing the injection pressure. Zhao et al. [19] studied the spray characteristics at different injection durations and injection pressure between 50 and 390 MPa by using four different injectors and found that the spray characteristics cannot be further improved when the injection pressure is higher than a critical value, which was in the range of 300–350 MPa. In addition, Chang et al. [20] was also found that the critical value of the injection pressure depended on the design of injectors. Therefore, it is necessary to explore a new way to improve the diesel spray characteristics under high injection pressure conditions.

On the other hand, it has been found that the in-nozzle flow and atomization characteristics of diesel engines were considerably influenced by nozzle geometries [21,22]. Taskiran [23] reported that using a nozzle with rounded hole inlets resulted in higher discharge coefficients compared with using a nozzle with sharp hole inlets. Suh et al. [24] investigated the effect of cavitation flow on the diesel fuel atomization characteristics in nozzles with different length to width (L/W) ratios and found that the longer nozzle orifice length induces enhancement of fuel atomization due to the lower discharge coefficient. Therefore, the optimization of the nozzle geometry structure is one of the most important and effective approaches to improve the spray characteristics [25–30].

In addition to optimizing the traditional hole nozzle, in recent years, the designs of several nonconventional hole geometries have been proposed, such as elliptical holes [27], group holes [28], and intersecting holes [29]. Some of the elliptical orifices can produce strong cavitation because of the vorticity magnitude and turbulence vortex structures [31]. Furthermore, the interchanging of the major axis and the minor axis can effectively enhance the air entrainment and improve the atomization quality of the fuel in the spray process [32–34]. Another interesting method is the use of group holes for nozzles. The spray of group-hole nozzles seemed to be more stable and gas entrainment was enhanced [35]. Compared to the single-hole nozzle under the same operation conditions, it can be found that the spray tip penetration of group-hole nozzles is longer than that of the single hole, resulting in improving the in-cylinder fuel–air mixing [28]. As one of the efforts in exploring the optimization of the nozzle hole geometry structure, the intersecting type hole nozzles were proposed by Long et al. [29] The intersecting type hole nozzles mainly include V-type intersecting hole nozzles and Y-type intersecting hole nozzles. In V-type intersecting hole nozzles, each hole is formed by the coalescence of a pair of subholes, while V-type intersecting hole nozzles with a disturbing domain are the Y-type intersecting hole nozzles, as displayed in Figure 1. In this figure, the axes of two or three subholes intersect at the surface of the nozzle tip, resulting in the intersecting type hole structure. The aim of this design is to utilize the internal impact effect of liquid fluids coming from the subholes to promote the breakup of liquid jets, accelerating liquid–gas mixing. Dong et al. [36] experimentally found that applying a V-type intersecting hole in a nozzle significantly improved the spray characteristics. Moreover, the particle size was found to decrease with the increase of the impact angle. Leng et al. [37,38] performed experimental and numerical investigations on the internal flow structure and mixing dynamics of V-type and Y-type intersecting hole nozzles, and found many vortex structures and high turbulent kinetic energy at the outlet field, which can improve the fuel atomization. Moreover, the sprays of intersecting hole nozzles are fan-shaped, which have a higher air entrainment rate than spray emerging from a cylindrical hole nozzle. These studies preliminarily show that intersecting hole nozzles have the potential to improve fuel–air mixing.

However, in all these numerical studies on intersecting hole type nozzles, the turbulence model used was Reynolds-averaged Navier–Stokes (RANS) model, which was not competent in resolving the detailed vortex structure of the flow field in and out of the nozzles. Moreover, the effects of the structural difference between V-type and Y-type intersecting hole nozzles on the

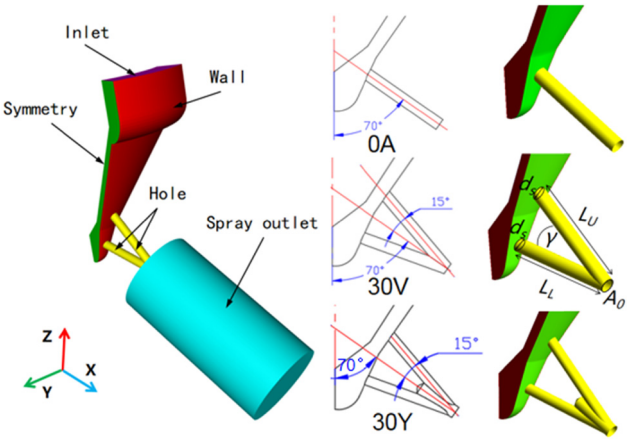

Figure 1: The geometry model of the nozzle and boundary definition.

breakup process of the jets have not been fully clarified. In fact, these vortex structures and differences in the nozzle structure can significantly influence the development and breakup of the jet [21–24]. On the other hand, large-eddy simulation (LES) is able to clarify more detailed vortex structures and temporal fluctuations of the turbulent flow behaviors both inside and outside of injector nozzles [39].

Therefore, in order to clarify the atomization characteristics of intersecting hole nozzles, especially the effects of the nozzle structure on the in-nozzle cavitating flow dynamics and thereby the initial breakup process of the jet near nozzles outlet, the LES method was employed to investigate the turbulent characteristics of the in- and out-nozzle multiphase flow field of V-type and Y-type intersecting hole nozzles, coupled with the VOF method that was used to describe phase transportation processes. Moreover, the characteristics of the jet breakup near the outer intersecting hole nozzles are quantitatively analyzed in terms of discharge coefficients, spreading angles, and the probability density function of the droplet diameters.

2 Mathematical models

2.1 Multiphase flow model

In order to capture the internal cavitating flow and atomization processes of a jet, a three-phase volume of fluid (VOF) model (fuel liquid, fuel vapor, and air) was introduced. The phase transport equations are as follows:

$$\frac{1}{\rho_l}\left[\frac{\partial}{\partial t}(\alpha_l\rho_l) + \nabla\cdot(\alpha_l\rho_l\vec{v}) = \dot{R}_c - \dot{R}_e\right] \quad (1)$$

$$\frac{1}{\rho_a}\left[\frac{\partial}{\partial t}(\alpha_a\rho_a) + \nabla\cdot(\alpha_a\rho_a\vec{v})\right] = 0 \quad (2)$$

$$\alpha_l + \alpha_v + \alpha_a = 1 \quad (3)$$

where $\dot{R}_c$ and $\dot{R}_e$ are the mass transfer rate according to condensation and evaporation; and α_l, α_v, and α_a are volume fractions of the liquid diesel, vapor diesel, and air phases, respectively. A single momentum equation is solved throughout the domain, so $\vec{v}$ is shared among the phase velocities. In the current study, the Zwart–Gerber–Belamri model [40] was used to describe the mass transfer process, including the cavitation of liquid diesel and the condensation of vapor diesel. The mass transfer rates of both phases are defined as follows:

$$\dot{R}_e = f_{vap}\frac{3\alpha_{nuc}(1-\alpha_v)\rho_v}{R_B}\sqrt{\frac{2}{3}\frac{(P_v - P)}{\rho_l}}, \quad P \le P_v \quad (4)$$

$$\dot{R}_c = f_{cond}\frac{3\alpha_v\rho_v}{R_B}\sqrt{\frac{2}{3}\frac{(P - P_v)}{\rho_l}}, \quad P \ge P_v \quad (5)$$

In these equations, there are two empirical calibration coefficients, the evaporation coefficient f_{vap} and the condensation coefficient f_{cond}, respectively. P_v is the saturated vapor pressure of the fuel, R_B is the radius of a bubble, and ρ is the density of a three-phase fluid mixture, which is defined as

$$\rho = \alpha_l\rho_l + \alpha_v\rho_v + \alpha_a\rho_a \quad (6)$$

2.2 Turbulence model

For the high Reynolds number flow, there are three main categories of approaches to model turbulence: direct numerical simulation (DNS), RANS, and large eddy simulation (LES). Because of the enormous computational cost of the simulation [41], DNS is not feasible for practical engineering problems. RANS [42–44] is widely used in industrial flow and heat transfer simulations, but it could not capture small eddies in the flow. In fact, these small eddies can significantly influence flow development. Different from DNS and RANS methods, in the LES method, large eddies are resolved directly, while small eddies are modeled. The LES method can capture the large-scale effect and eddies' structure in the nonequilibrium process, which is beyond the capability of the RANS method. Moreover, it overcomes the enormous computational cost caused by the need to solve all turbulence scales in DNS. Therefore, in this work, the LES method is used to describe the turbulence, and the WALES subgrid scale turbulence model [45] is employed.

2.3 Nozzle geometries and meshes

A numerical investigation was performed on three eight-hole micro-sac nozzles with V-type intersecting holes, Y-type intersecting holes, and regular cylindrical holes as a reference. To save computing cost, meshes are created for 1/8th of the entire nozzle, containing only one hole. As shown in Figure 1, the cylindrical hole nozzle is denoted as nozzle 0A. The V-type intersecting hole nozzle is denoted as 30V according to the impact angle of 30°. The V-type intersecting hole nozzle with the disturbing domain is the Y-type intersecting hole nozzle, denoted as

Table 1: Geometric parameters of the nozzle holes

Item	0A	30V	30Y
Subhole impact angle (γ, deg)	0	30	30
Subhole diameter (d_s, mm)	0.2	0.2	0.16
Upper subhole length (L_U, mm)	1.5	1.5	1.5
Lower subhole length (L_L, mm)	1.5	1.5	1.5
Outlet area (A_0, $\times 10^{-8}$ m^2)	3.14	3.14	3.14

30Y. Meanwhile, the spray chamber is added downstream of the hole exit to provide initial boundary conditions for the jet. The geometrical parameters about all of the nozzles have been listed in Table 1, and the operating conditions are listed in Table 2.

The Taylor microscale is usually used to describe the scale characteristics of the turbulent vortex. In this study, the Taylor microscale can be approximated by the following equation [46]:

$$\lambda_g = \sqrt{\frac{10}{\mathrm{Re}}} D \tag{7}$$

where Re is the Reynolds number and D is the diameter of the nozzle hole. According to this equation, the Taylor microscale of the nozzles in the current study is estimated as 3 μm. As a result, it was found that the grid size in the orifice should vary from approximately 1 μm in the boundary region to 3.5 μm in the core region. The initial minimum grid size in the spray chamber was set to 1.1 μm near the interface between the liquid and the air. Finally, the number of cells was approximately 12,000,000 for 30V and 30Y nozzles and 9,200,000 for the 0A nozzle, as shown in Figure 2.

A physical variable, $\mathrm{LESIQ_v}$, was employed to assess the resolution quality of cells used in LES [47–49]:

$$\mathrm{LESIQ_v} = \frac{1}{1 + 0.05\left(\frac{\mu + \mu_t}{\mu}\right)^{0.53}} \tag{8}$$

where μ_t is the subgrid scale viscosity introduced by the WALES model. As seen from the equation, the $\mathrm{LESIQ_v}$ values ranges from 0 to 1, and it presents the ratio of the turbulent kinetic energy resolved by the LES to the total turbulent kinetic energy. Usually, it is believed that the $\mathrm{LESIQ_v}$ should be higher than 0.8 in LES [47]. The spatial distribution of the values of $\mathrm{LESIQ_v}$ at 20 μs after the start of injection is shown in Figure 3. It can be observed that the $\mathrm{LESIQ_v}$ values are higher than 0.92 for all the computing domains, indicating a high resolution of the meshes in the current study.

Table 2: Operating conditions

Item	Value
Injection pressure	150 MPa
Ambient pressure	0.1 MPa
Temperature	300 K
Gas	Air
Fuel	Diesel

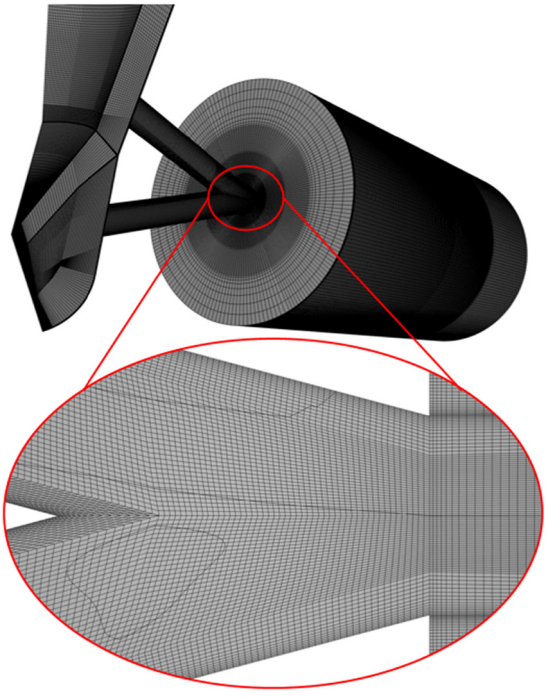

Figure 2: Detail of the meshes in the computational domain.

The LES turbulence model was coupled with the VOF model, and the ZGB cavitation model was employed. The SIMPLEC algorithm was employed to solve the velocity–pressure coupling equations. The bounded central differencing scheme was selected for the discretization of the momentum equation. The discretization of the volume fraction transport equation was used in the compressive

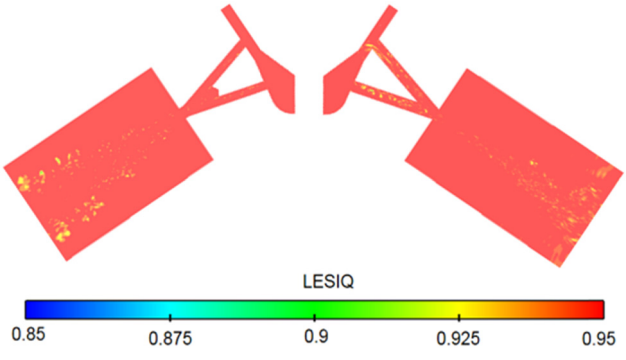

Figure 3: Evaluation of mesh resolution.

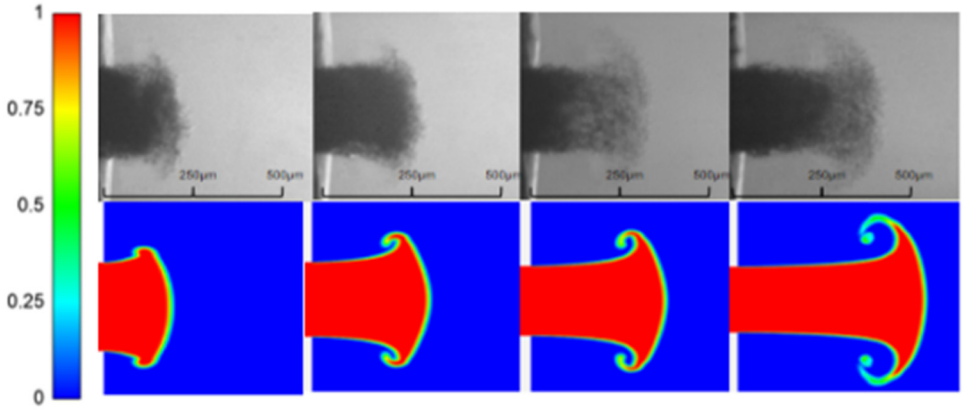

(a)

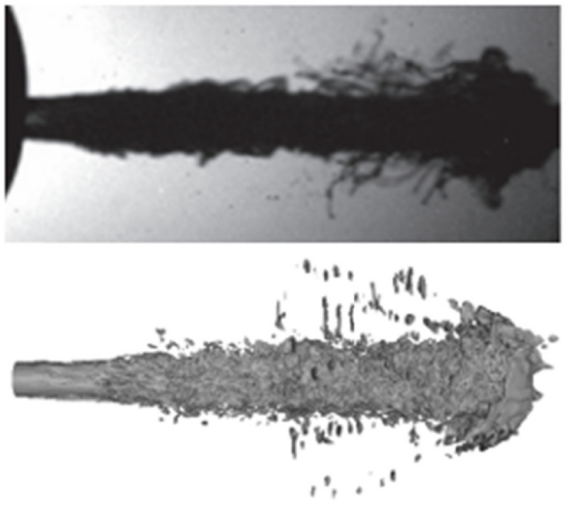

(b)

Figure 4: Comparison of numerical and experimental results including (a) the initial state of injection [54] and (b) the fully developed cavitation jet [53,54].

scheme. The cell gradients were calculated by using the least-squares cell-based method. Finally, the time integration was performed adopting the bounded second-order implicit scheme, and the time step was 1×10^{-9} s. The computations were implemented in commercial numerical software Fluent (ANSYS INC, 2019).

The numerical models have been extensively validated in previous investigations associated with the nozzle internal flow [48,50,51]. In this article, the numerical results were compared with the experimental results of Ghiji et al. [52] and Wang et al. [53,54]. Figure 4 shows a comparison of the numerical results with the experimental results using the LES-VOF method at different stages of the developing injection flow nearby the nozzle exit. At the initial stage of the injection, a mushroom-shaped jet tip is observed ins the experimental images, and the numerical results reproduced this structure (Figure 4a). As illustrated in Figure 4b, the cavitation is fully developed and significantly influences the spray structure. Overall, the LES-VOF model shows a good agreement between numerical and experimental results with different states of the internal flow and transient flow feature outside the nozzle. The properties of the liquid and vapor phases of diesel fuel are listed in Table 3.

Table 3: Properties of diesel fuel

Item	Liquid	Vapor	Air
Density (kg·m^{-3})	832	0.1361	1.165
Viscosity (Pa·s)	0.003	7×10^{-6}	1.86×10^{-5}
Saturation vapor pressure (Pa)	2,000		

3 Results and discussion

3.1 Nozzle geometries and meshes

As shown in Figure 5, the mass flow rates of the steady injection stage of 30V nozzle, 30Y nozzle, and 0A nozzle are 12.6 g·s^{-1}, about 11.3 g·s^{-1}, and 9.1 g·s^{-1}, respectively. Although these nozzles have the same outlet area, the mass flow rates of the 30V nozzle and the 30Y nozzle are significantly higher than that of the 0A nozzle. In addition, the dimensionless numbers used to characterize the flow characteristics in the nozzle are the discharge coefficient C_d, the area coefficient C_a, and the velocity coefficient C_v, which correspond to the global loss, area loss, and velocity loss of the nozzle, respectively [37,38]. A higher flow coefficient means less loss. These coefficients are defined in Eqs. 7–9:

$$C_d = \frac{\dot{m}_f}{A_0\sqrt{2\rho_l \Delta P_0}} \tag{9}$$

$$C_v = \frac{u_{eff}}{u_{th}} = \frac{u_{eff}}{\sqrt{2\Delta P_0/\rho_l}} \tag{10}$$

$$C_a = \frac{A_{eff}}{A_0} \tag{11}$$

where ρ_l is the density of liquid fuel, $\dot{m}_f$ is the mass flow, $\dot{M}_f$ is the momentum flux, and ΔP_0 is the difference of injection and discharge pressure over the nozzle. u_{eff} and A_{eff} are the effective velocity and the effective area of a hole, respectively; which are calculated as follows:

$$u_{eff} = \frac{\dot{M}_f}{\dot{m}_f} \tag{12}$$

$$A_{eff} = \frac{\dot{m}_f}{\rho_l \dot{M}_f} \tag{13}$$

Figure 6 shows the numerical results of the various flow coefficients for the three types of hole nozzles for the discharge coefficient C_d. The C_d values of the intersecting hole nozzle are 24–37% higher than those of the cylindrical hole nozzle.

The area coefficients C_a of the 30V nozzle and the 30Y nozzle are about 37% higher than that of the 0A nozzle due to noncavitation and a decrease in the area loss. It should be noticed that for the 30V nozzle, its area coefficient will be less than 1 because the velocity distribution is not uniform at the 30V nozzle outlet, even if there is no cavitation in the 30V nozzle. A similar phenomenon can also be found in the study of a tapered hole nozzle in ref. [55].

The velocity coefficients $C_v$for the 0A nozzle and the 30V nozzle are very close, which are 0.875 and 0.871, respectively. The velocity coefficient of the 30Y nozzle is 0.702, which is 24% lower than that of the 30V nozzle, and the reasons will be discussed in the next paragraph.

Due to the noncavitation flow characteristics of the intersecting hole nozzles, the discharge coefficient of the intersecting hole nozzles is much higher than that of the cylindrical hole nozzle and greatly reduces the area loss of the flow over nozzles. This result is consistent with previous studies [24]. The higher discharge coefficient is beneficial to improve the atomization and mixing rate because of lower global energy loss at nozzles and the possibility of reducing the hole dimension in a given mass flow requirement [56].

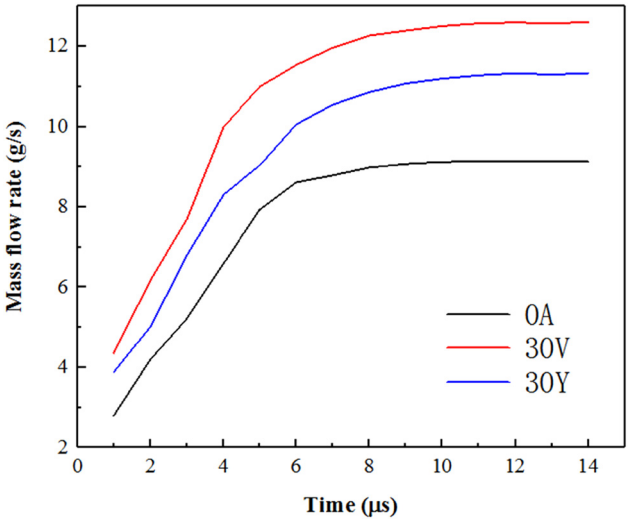

Figure 5: Mass flow rates of nozzles.

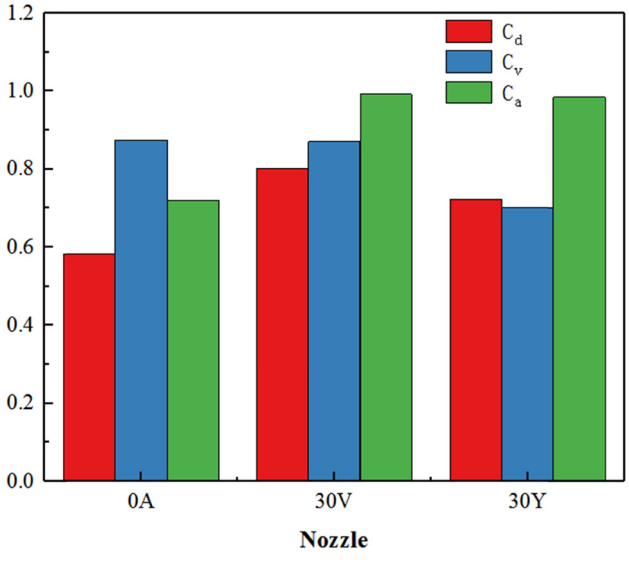

Figure 6: Velocity and area coefficients for nozzles 0A, 30V, and 30Y.

3.2 Spatial distribution of the flow parameters

The differences of the cross area-averaged pressure at various axial positions from the nozzle exit for the 0A, 30V, and 30Y nozzles can be clearly seen from Figure 7. For the 0A nozzle, the pressure drops by 95% within 0.2 mm near the inlet and then remains at about 0.1 MPa until the outlet. The axial pressure distribution in the 0A nozzle presents an L-shape, so there is a great pressure gradient near the inlet. The 30V and the 30Y nozzles have a similar axial pressure distribution: it shows a stepped shape with a decrease in the pressure near the inlet and outlet. For the 30V nozzle, the pressure decreases by 25% within 0.2 mm near the inlet and remains at about 90 MPa in 0.3–1.1 mm. Finally, the pressure decreases to 19 MPa in 1.1–1.5 mm near the outlet. However, there are some differences in the pressure distribution of 30Y; the pressure of the 30Y nozzle decreases by 71% within 0.2 mm and then remains at about 50 MPa, and finally, decreases to 0.1 MPa in 1.1–1.5 mm. In order to ensure the same outlet diameter, the 30Y inlet diameter is smaller than the 30V inlet diameter. As a result, the pressure gradient of the 30Y nozzle is significantly higher than that of the 30V nozzle near the inlet.

As shown in Figure 8, for the 0A nozzle, the cavitation appears under 150 MPa of the injection pressure and develops from the inlet to the outlet of the hole, while for the intersecting hole nozzles, cavitation hardly appears. Due to the overall convergent hole structure, the pressure of the intersecting hole nozzles decreases near the inlet and outlet, which reduces the pressure gradient of a single local area. Therefore, the intersecting hole nozzles can effectively restrain cavitation.

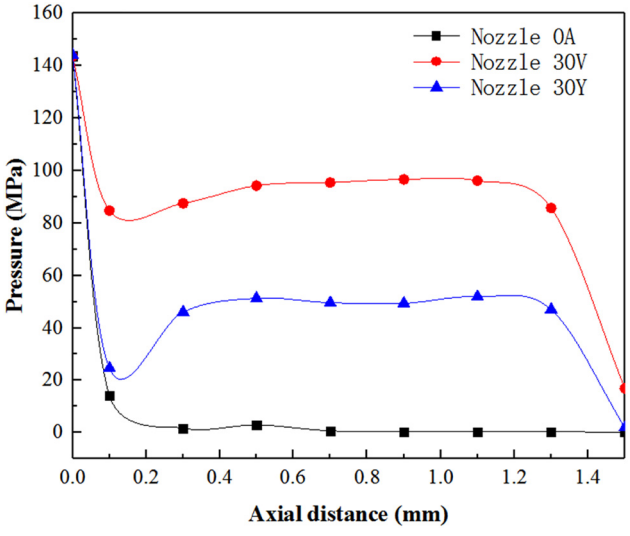

Figure 7: Axial pressure distribution at the hole.

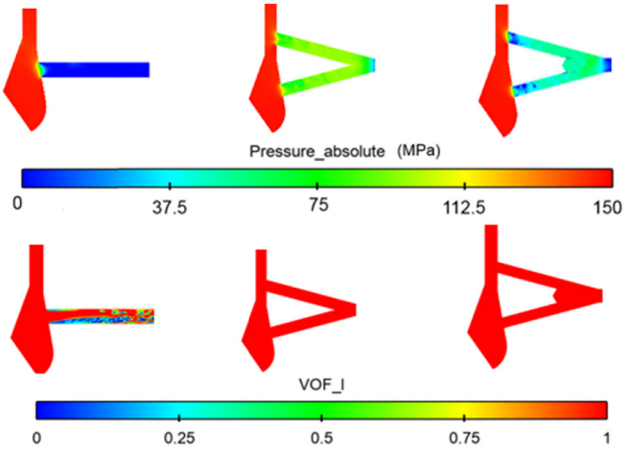

Figure 8: Pressure and liquid volume of the fraction at the hole.

To understand the development of the cavitation in the 30Y nozzle outlet, the three-phase (liquid, vapor, and air) volume fraction distributions and vector fields are depicted in Figure 9. It can be seen that the cavitation appears near the upper and lower parts of the outlet, at 4 μs after the start of injection (ASOI). As a result, the nozzle outlet is full with diesel liquid and diesel vapor. Then, the diesel vapor disappears in the upper and lower parts of the outlet, at 10 μs ASOI. But, the diesel liquid is not filled with the outlet, and the upper and lower parts of the outlet are filled by air. The vector field of the liquid phase at 10 μs ASOI is shown in Figure 9b; it can be seen that reverse vortices occur at the outlet of the hole. The air suction appears after cavitation disappeared in the upper and lower parts of the outlet, which is only observed in the 30Y nozzle. In other words, the air suction causes a jet emerging from the 30Y nozzle very different from a jet emerging from the 30V nozzle. That is why the flow over the 30Y nozzle has a higher velocity loss. The jet emerging from the 30Y nozzle was disturbed and swung strongly near the outlet. Furthermore, the effect of air suction will be discussed in the later part.

3.3 Velocity fields in the nozzle outlet

Further details regarding the full development flow of 0A, 30V, and 30Y in the outlet, including the flow fields and the cavitation distributions on the cutting plane perpendicular to the jet axis are shown in Figure 10. Since the velocity of the diesel vapor is smaller than that of the diesel liquid, two vortices around the diesel vapor region

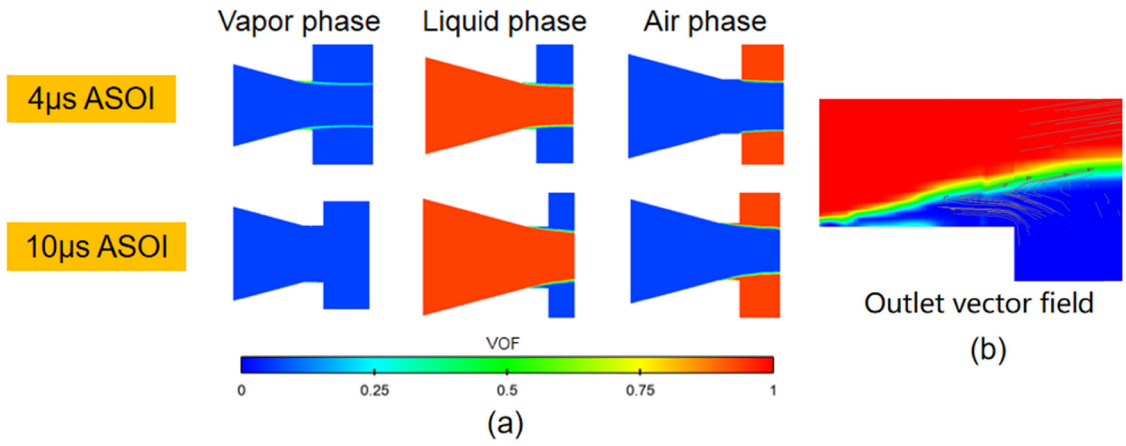

Figure 9: Development of the 30Y nozzle jet at the nozzle outlet.

are generated at the 0A nozzle outlet. For the 30V nozzle, there is no cavitation or air suction at the outlet, but a small vortex is present in the middle of the hole caused by the collision and impact of the fuel in two subholes of the intersecting hole nozzle. Furthermore, the velocity is more uniform at the 30V nozzle outlet. Unexpectedly, there are four vortices at the 30Y nozzle outlet, which are on both sides of the upper and lower air suction regions. Additionally, the velocity in the upper part of the outlet is slightly lower than that in the lower part of the outlet. The internal flow of intersecting hole nozzles is more complex because of the collision and impact of the fuel. The turbulence flow is an important reason to induce fluctuation on the jet surface and then breakup

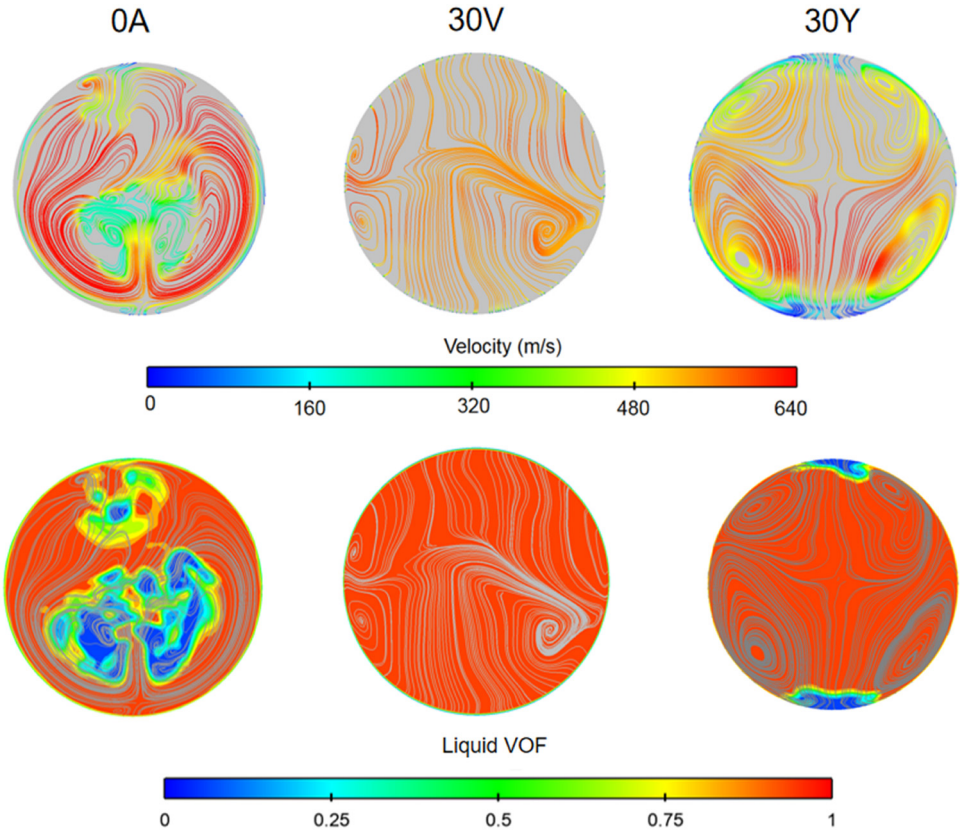

Figure 10: Comparison of the outlet velocity fields.

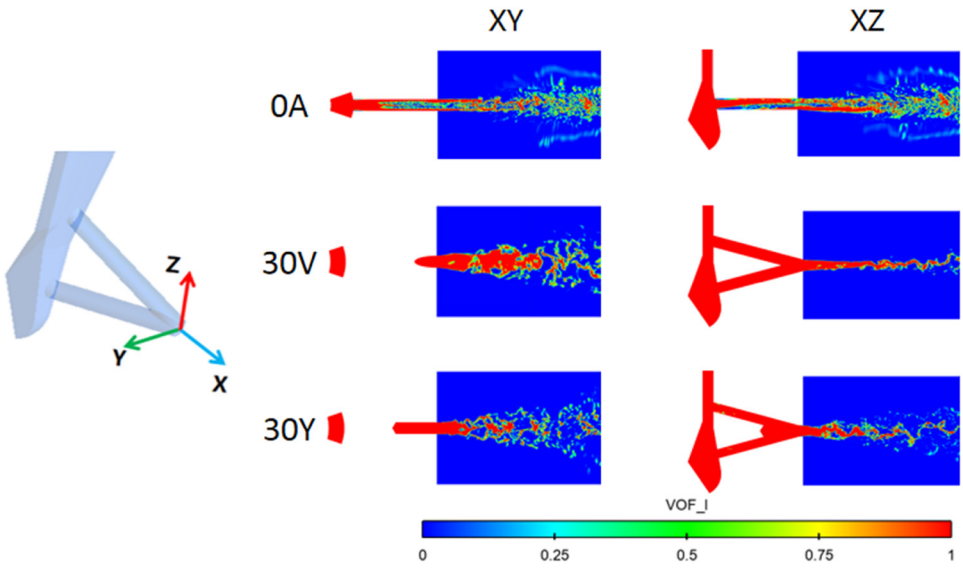

Figure 11: Spatial distribution of the liquid volume fraction on the *XY*-plane and the *XZ*-plane.

jets [57]. Therefore, the impact turbulence flow will promote jet atomization.

3.4 Spreading angles

Figure 11 shows the spatial distribution of the liquid volume fraction for nozzles 0A, 30V, and 30Y. More detailed structures of the jet are given on the *XY*-plane and the *XZ*-plane, respectively. It can be observed that for the 0A nozzle, there is minimal mixing in the near-field. The 30V and 30Y nozzles have a larger spreading angle on the *XY* plane. It can be seen from Figure 12 that the spreading angle of the 30V and 30Y nozzles is about 35°, while that of the 0A nozzle is only about 20° on the *XY* plane. In other words, the spreading angle is about 1.5 times wider than that of the cylindrical nozzle on the *XY* plane. On the *XZ* plane, the spray angle of the 30V nozzle is 11°, which is slightly lower than that of the 0A nozzle, while the spreading angle of the 30Y remains at a larger value of 41°. It can be also observed from the *XZ* plane that the jet of the 30Y nozzle has a strong fluctuation and disturbance at the outlet because of air suction. As a result, some liquid ligaments and droplets separate from the main jet; then, the surface wave caused by the jet fluctuation propagates to the spray downstream and promotes the jet breakup. In addition, a similar jet fluctuation phenomenon is observed in the 30V nozzle jet, but only in the downstream of the jet and the fluctuation is weak. In conclusion, setting the blind hole as the disturbing domain improves the spreading angle and enhances atomization.

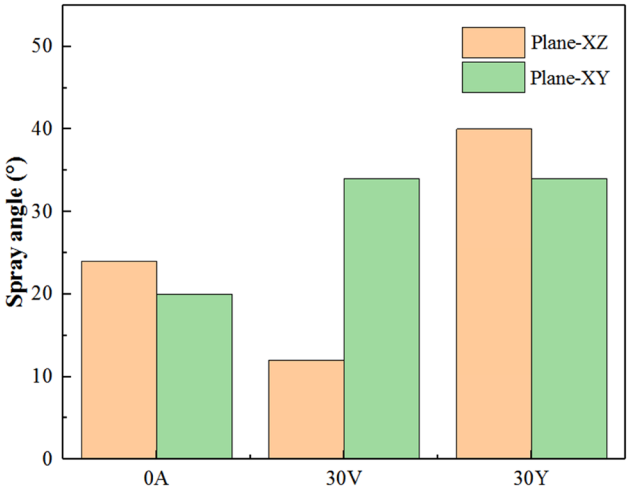

Figure 12: Spray angle of nozzles on the *XY*-plane and the *XZ*-plane.

3.5 Droplet statistics

In order to characterize the jet development, the droplet size and droplet velocity distributions were calculated for three different positions in the spray chamber. These positions were located at 0.5, 1.5, and 2.5 mm downstream of the nozzle outlet and denoted here as M1, M2, and M3, respectively. The location where M1–M3 is located is depicted in Figure 13.

In order to calculate droplet size statistics, a threshold of $\alpha_l > 0.5$ was used to characterize liquid regions for each slice M1–M3. Then, to separate the connected liquid

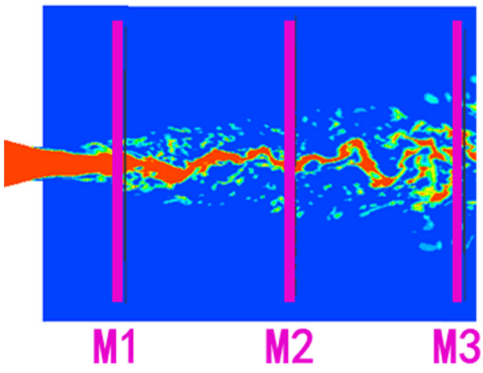

Figure 13: Positions M1–M3 where droplet size distributions are calculated.

fragments, an erosion operation was performed. Thereby, the size of the erosion operator equaled two times the mesh size. In the next step, dilatation was performed again with an operator size two times the mesh size. Next, the droplets were counted and sorted by the diameter. Finally, the droplet number based on the probability density function (PDF) was calculated. This postprocessing method has been validated in ref. [58].

Figure 14 gives the droplet size distribution for different locations M1–M3. A general trend can be found in Figure 14a–c. The droplets are large near the nozzle outlet and become smaller with an increase in the distance. Therefore, the peak value of the droplet size distribution shifts toward smaller droplet diameters. However, there are some differences among the droplet size

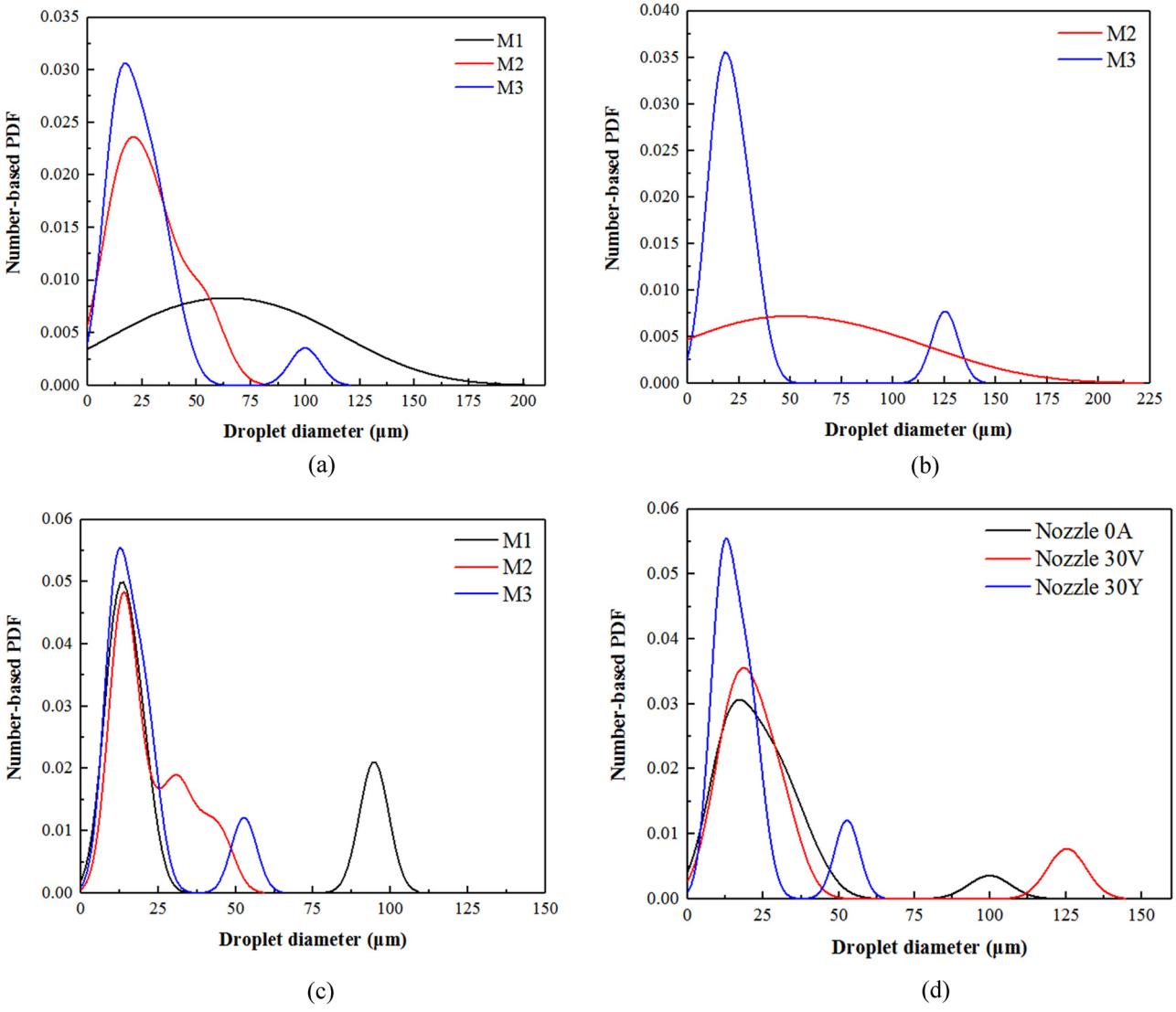

Figure 14: Droplet size distribution at different locations downstream of the nozzles. The droplet size distribution of the (a) 0A nozzle, (b) 30V nozzle, (c) 30Y nozzle; and (d) at M3.

distribution of the three nozzles. For the 0A nozzle, with an increase of the distance, the PDFs of small droplets increased gradually, while the most obvious change of the droplet diameter is the 30V nozzle. Since the jet diameter is almost 130 μm and not broken at M1, the PDFs of the droplet at M1 are not shown in Figure 14b. However, with the increase in the distance, the jet is rapidly broken. As a result, the number of small droplets increases rapidly. At M3, only a small portion of the jet is not broken and most of the droplet diameter is 25 μm. For the 30Y nozzle, the droplets' diameter of about 20 μm remains the most even at M1. With the increase of the distance, the PDFs of small droplets still remain at a higher value. The droplet size distribution of three nozzles at M3can be observed in Figure 14d. Obviously, the jet emerging from the 30V nozzle had a high breakup rate and the mean droplet diameter was 19.78 μm. The droplet size distribution of the 30Y nozzle was slightly better than that of the 0A nozzle. However, the mean droplet diameter of the 0A nozzle was 27.06 μm, while the mean droplet diameter of 30V was 33.06 μm.

Figure 15 shows the predicted droplet velocity distributions at different locations M1–M3 for nozzles 0A, 30V, and 30Y, respectively. By comparing Figure 15a–c, it can be found that the droplet velocity distribution of the intersecting hole nozzle is obviously different from that of the cylindrical hole nozzle. When the jets moved downstream, the droplet of velocity tends to decrease. For intersecting hole nozzles, the velocity of droplets is concentrated at about 550–600 $m \cdot s^{-1}$ at M1, while the velocity of most droplets sharply decreased to 200–300 $m \cdot s^{-1}$ at M3. However, in the case of the cylindrical hole nozzle, with the jets moving downstream, the droplet velocity distribution tends to be slightly decreased. The droplet velocity of cylindrical hole nozzles is dispersed at M1 but the velocity of some droplets decreased to 200–300 $m \cdot s^{-1}$ at M3. The reason may be that the surface area of the fan-shaped jet emerging from the intersecting hole nozzle is larger than that of a cylindrical hole nozzle. Therefore, the aerodynamic effect of the fan-shaped jet emerging from the intersecting hole nozzle is stronger than that of a cylindrical hole nozzle, and with the jets moving downstream, the jet broke up to more small droplets, and the PDF of low-velocity droplets increased.

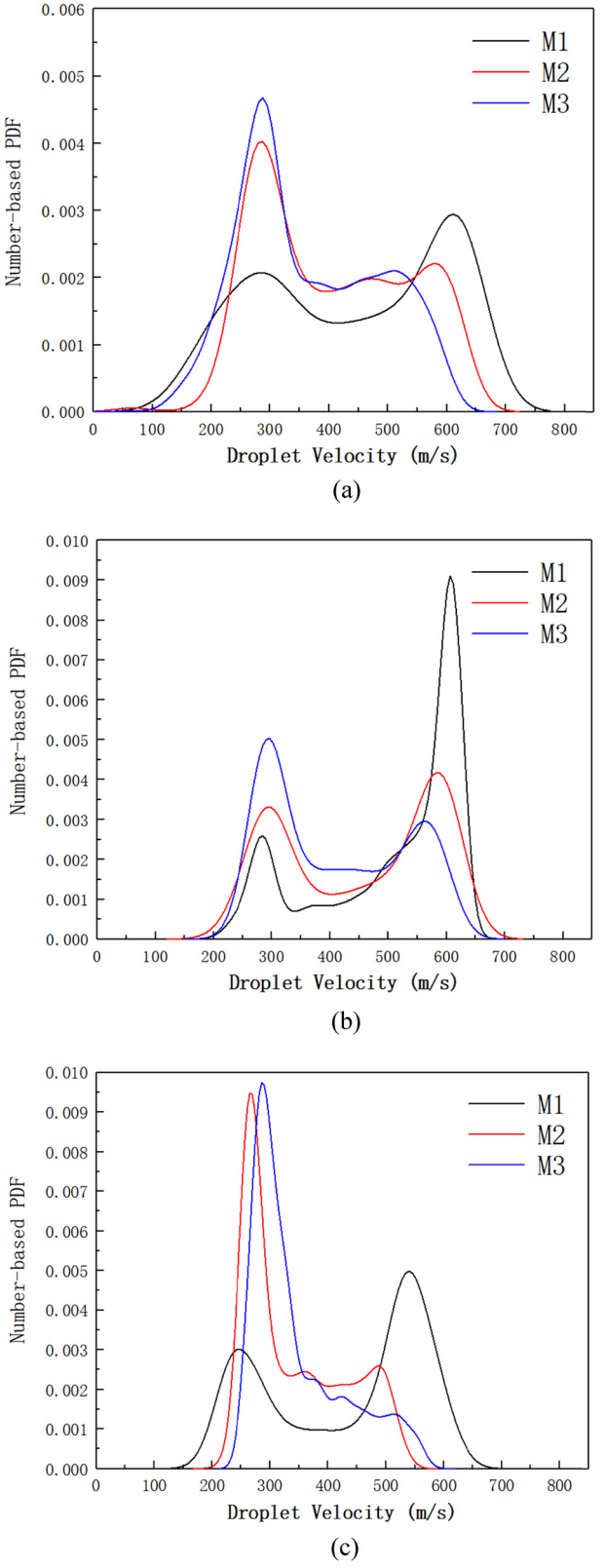

Figure 15: Droplet velocity distribution at different locations downstream of the nozzles. The droplet velocity distribution of the (a) 0A nozzle, (b) 30V nozzle, and (c) 30Y nozzle.

3.6 *Q*-Criterion

In this article, *Q*-criterion is used to capture vortex structures. When the value of the *Q*-criterion is positive, the

vortex tensor of the fluid is greater than the strain rate tensor. The vorticity close to the center of the vortex should increase, so the Q is expected to remain a positive value in the core of the vortex. Therefore, the regions with positive Q indicate vortex structures in a flow field. The Q-criterion is defined as follows:

$$Q = \frac{1}{2}(\Omega_{ij}\Omega_{ij} - S_{ij}S_{ij}) \tag{14}$$

where

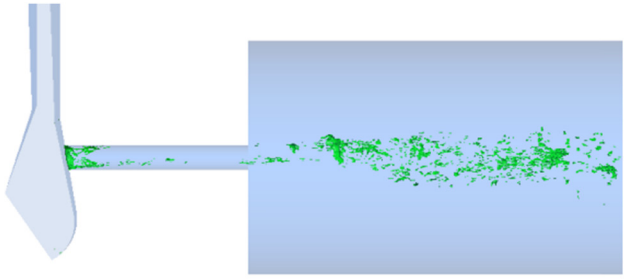

(a)

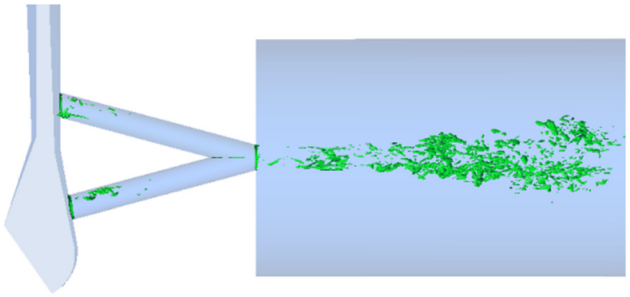

(b)

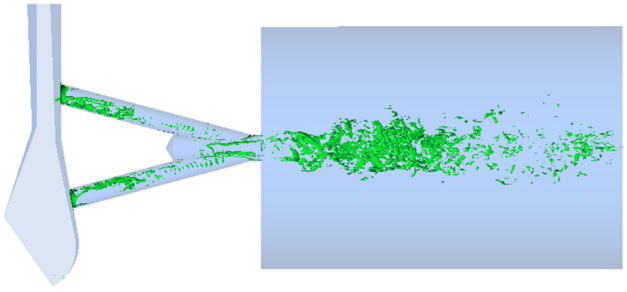

(c)

Figure 16: Comparison of the isosurface of Q in different nozzles. The isosurface of Q in the (a) 0A nozzle, (b) 30V nozzle, and (c) 30Y nozzle.

$$\Omega_{ij} = \frac{1}{2}\left(\frac{\partial u_i}{\partial x_j} - \frac{\partial u_j}{\partial x_i}\right) \tag{15}$$

$$S_{ij} = \frac{1}{2}\left(\frac{\partial u_i}{\partial x_j} + \frac{\partial u_j}{\partial x_i}\right) \tag{16}$$

In Figure 16, distributions of lumps of the isolated vortex surfaces of $Q = 2 \times 10^{14}$ in the hole and the spray domain are indicated. Obviously, a large number of isolated vortex surfaces were observed around the downstream spray field region and the upstream spray field region in the 30V nozzle and the 30Y nozzle, respectively. Therefore, the jet of the 30Y nozzle was disturbed near the outlet and broke up early. Although the jet of the 30V nozzle broke later, the breakup rate was high in the downstream spray field. On the other hand, a few isolated vortex surfaces were observed in the 0A nozzle hole and the spray field, as shown in Figure 16a. As a result, the formation of isolated vortex surfaces validates that the instability of jet in intersecting hole nozzles is much larger than that in cylindrical hole nozzles.

4 Conclusion

In this article, the multiphase flow inside and outside the nozzle was numerically simulated using a VOF-LES method to clarify the effects of the nozzle structure on the cavitation flow and primary atomization characteristics for cylindrical, V-type, and Y-type intersecting hole nozzles at 150 MPa injection pressure and 0.1 MPa back pressure. The simulation results agree well with the experimental data in this work. The main conclusions in this study are summarized as follows:

1. The global loss and area loss of the flow over an intersecting type hole nozzle are lower than those of a cylindrical hole nozzle, while the flow over the Y-type intersecting hole nozzle has a higher velocity loss among the three nozzles.
2. For the cylindrical hole nozzle, the pressure distribution is of L-shape along the hole; while for the intersecting hole nozzles, the pressure shows a stepped shape drop along the holes due to the overall convergent hole structure. The pressure of intersecting hole nozzles decreases near the inlet and outlet, which reduces the pressure gradient of a single local area. Therefore, the intersecting hole nozzles have a great potential for inhibiting cavitation.
3. A fan shape can be observed in the near-field region of the intersecting hole nozzles. The aerodynamic effect

can significantly affect the distribution of droplet velocity at different locations. The jet emerging from intersecting hole nozzles shows wider spreading angles and smaller droplet sizes.

4. Since the blind hole is set as the disturbing domain, the jets emerging from a Y-type intersecting hole nozzle are more disturbed and unstable, leading to enhanced atomization.

Funding information: This research was supported by the Jiangsu Provincial Key Research and Development Program, China (BE2019009-5), the National Natural Science Foundation of China (grant number 51776088, 51779044, 51876083), and a Project Funded by the Priority Academic Program Development of Jiangsu High Education Institutions.

Author contributions: Xianyin Leng: writing – review and editing, resources; Yicheng Deng: writing – original draft, formal analysis, visualization; Wei Guan: formal analysis; Zhixia He: resources; Wuqiang Long: methodology; Shengli Wei: resources; Jie Hu: writing – review and editing.

Conflict of interest: The authors state no conflict of interest.

References

[1] Shah KJ, Pan SY, Lee I, Kim H, You Z, Zheng JM, et al. Green transportation for sustainability: review of current barriers, strategies, and innovative technologies. J Clean Prod. 2021;326:129392.

[2] Xu O, Min X. Promoting green transportation under the belt and road initiative: locating charging stations considering electric vehicle users' travel behavior. Transp Policy. 2022;423:58–80.

[3] Li Z, Wang C, Quan L, Hao Y, Xia L. Study on energy efficiency characteristics of the heavy-duty manipulator driven by electro-hydraulic hybrid active-passive system. Autom Constr. 2021;125(7):103646-260.

[4] Saidani M, Yannou B, Leroy Y, Cluzel F. Heavy vehicles on the road towards the circular economy: analysis and comparison with the automotive industry. Resour Conserv Recycling. 2017;135:108–22.

[5] Radpour S, Gemechu E, Ahiduzzaman M, Kumar A. Developing a framework to assess the long-term adoption of renewable energy technologies in the electric power sector: the effects of carbon price and economic incentives. Renew Sustain Energy Rev. 2021;152:111663.

[6] Swp A, Ksc B, Gh C, Sys B. Electric vehicle charging management using location-based incentives for reducing renewable energy curtailment considering the distribution system. Appl Energy. 2022;305:117680.

[7] Magotra VK, Kang TW, Ahmed A, Inamdar AI, Kumar S. Effect of gold nanoparticles laced anode on the bio-electro-catalytic activity and power generation ability of compost based microbial fuel cell as a coin cell sized device. Biomass Bioenergy. 2021;152(9):106200.

[8] Tozlu A. Techno-economic assessment of a synthetic fuel production facility by hydrogenation of CO_2 captured from biogas. Int J Hydrog Energy. 2022;47:5.

[9] Wang X, Hoekman SK, Han Y, Chow JC, Schuetzle R. Potential emission reductions by converting agricultural residue biomass to synthetic fuels for vehicles and domestic cooking in china. Particuology. 2019;49:40–7.

[10] Zhao W, Yan J, Gao S, Lee TH, Li X. The combustion and emission characteristics of a common-rail diesel engine fueled with diesel, propanol, and pentanol blends under low intake pressures. Fuel. 2022;307:121692.

[11] Ju K, Kim J, Park J. Numerical prediction of the performance and emission of downsized two-cylinder diesel engine for range extender considering high boosting, heavy exhaust gas recirculation, and advanced injection timing – sciencedirect. Fuel. 2021;302:121216.

[12] Dong Q, Yang X, Ni H, Song J, Ni Z. An on-line measurement method of injection rate of high pressure common rail system. Measurement. 2020;170(3):108716.

[13] Song LB, Liu T, Fu W, Lin QZ. Experimental study on spray characteristics of ethanol-aviation kerosene blended fuel with a high-pressure common rail injection system. J Energy Inst. 2018;91(2):203–13.

[14] Achebe CH, Ogunedo B, Chukwuneke JL, Anosike NB. Analysis of diesel engine injector nozzle spray characteristics fueled with residual fuel oil. Heliyon. 2020;6(8):e04637.

[15] Yang ZM, Lee HT, Li YK, Chen WT, Zhang YH. Spray and combustion characteristics of pure hydrothermal liquefaction biofuel and mixture blends with diesel. Fuel. 2021;294:120498.

[16] Cao DN, Hoang AT, Luu HQ, Bui VG, Tran TTH. Effects of injection pressure on the NOx and PM emission control of diesel engine: a review under the aspect of PCCI combustion condition. Energy Sources, Part A: Recovery, Utilization, Environ Eff. 2020. doi: 10.1080/15567036.2020.1754531.

[17] Hiroyasu H, Arai M. Structures of fuel sprays in diesel engines. International Congress & Exposition; 1990.

[18] Zhang QH, Hao ZY, Zheng X, Yang WY, Mao J. Mechanism and optimization of fuel injection parameters on combustion noise of DI diesel engine. J Cent South Univ. 2016;23(02):379–93.

[19] Zhao J, Grekhov L, Yue P. Limit of fuel injection rate in the common rail system under ultra-high pressures. Int J Automot Technol. 2020;21(3):649–56.

[20] Chang Z, Yu J, Nishida K, Ogata Y. Diesel spray and combustion of multi-hole injectors with micro-hole under ultra-high injection pressure–non-evaporating spray characteristics. Fuel. 2021;283:119322.

[21] Balz R, Bernardasci G, Rotz BV, Sedarsky D. Influence of nozzle geometry on spray and combustion characteristics related to large two-stroke engine fuel injection systems. Fuel. 2021;294:294.

[22] He ZX, Shao Z, Wang Q, Zhong WJ. Experimental study of cavitating flow inside vertical multi-hole nozzles with different length–diameter ratios using diesel and biodiesel. 2015;60:252–62.

[23] Taskiran OO. Investigation of the effect of nozzle inlet rounding on diesel spray formation and combustion. Fuel. 2018;217:193–201.
[24] Suh H, Lee C. Effect of cavitation in nozzle orifice on the diesel fuel atomization characteristics. Int J Heat Fluid Flow. 2008;29(4):1001–9.
[25] Xiao JB, Yan HJ, Schubert M, Unger S, Hampel U. Effect of nozzle geometry on pressure drop in submerged gas injection. J Cent South Univ. 2019;26(8):2068–76.
[26] Nandakumar C, Raman V, Saravanan CG, Vikneswaran M, Thirunavukkarasu M. Effect of nozzle hole geometry on the operation of kapok biodiesel in a diesel engine. Fuel. 2020;276:118114.
[27] Hong J, Ku K, Kim S, Lee C. Effect of cavitation in circular nozzle and elliptical nozzles on the spray characteristic. Atomization Sprays. 2010;20:877–86.
[28] Lee S, Park S. Spray atomization characteristics of a GDI injector equipped with a group-hole nozzle. Fuel. 2014;137:137–59.
[29] Long WQ, Leng XY, Tian JP, Dong Q, Wei SL, Qi LP, et al. The intersecting hole nozzle with a disturbing domain; 2011, 2.2, China, ZL200810012342X. in Chinese.
[30] He ZX, Zhang ZY, Guo GM, Wang Q, Leng XY. Visual experiment of transient cavitating flow characteristics in the real-size diesel injector nozzle. Int Commun Heat Mass Transf. 2016;78:13–20.
[31] Yu SH, Yin BF, Jia HK, Wen S, Li X, Yu J. Theoretical and experimental comparison of internal flow and spray characteristics between diesel and biodiesel. Fuel. 2017;208:20–9.
[32] Amini G, Dolatabadi A. Capillary instability of elliptic liquid jets. Phys Fluids. 2011;23(8):084109.
[33] Matsson A, Jacobsson L, Andersson S. The effect of elliptical nozzle holes on combustion and emission formation in a heavy duty diesel engine. SAE Technical Paper; 2000.
[34] Molina S, Salvador F, Carreres M, Jaramillo D. A computational investigation on the influence of the use of elliptical orifices on the inner nozzle flow and cavitation development in diesel injector nozzles. Energy Convers Manag. 2014;79(3):114–27.
[35] Moon S, Matsumoto Y, Nishida K, Jian G. Gas entrainment characteristics of diesel spray injected by a group-hole nozzle. Fuel. 2010;89(11):3287–99.
[36] Dong Q, Long WQ, Ishima T, Kawashima H. Spray characteristics of V-type intersecting hole nozzles for diesel engines. Fuel. 2013;104:500–7.
[37] Leng XY, Jin Y, He ZX, Long WQ, Nishida K. Numerical study of the internal flow and initial mixing of diesel injector nozzles with V-type intersecting holes. Fuel. 2017;197:31–41.
[38] Leng XY, Jin Y, He ZX, Wang Q, Li M, Long WQ. Effects of V-type intersecting hole on the internal and near field flow dynamics of pressure atomizer nozzles. Int J Therm Sci. 2018;130:183–91.
[39] Guo GM, He ZH, Lia MC, Duan XB, Leng XY, Duan L. Optical experiment and large eddy simulation on effects of in-nozzle stagnant air bubbles and diesel on near-nozzle spray structure variation in diesel injector. Fuel. 2019;255:115721.
[40] Zwart PJ, Gerber AG, Belamri T. A Two-Phase Flow Model for Predicting Cavitation Dynamics. In Proceedings of the Fifth International Conference on Multiphase Flow. Yokohama, Japan: 2004.
[41] Guan W, He ZX, Zhang L, Guo GM, Leng XY. Investigations on interactions between vortex flow and the induced string cavitation characteristics in real-size diesel tapered-hole nozzles. Fuel. 2021;287(2):119535.
[42] Launder BE, Spalding DB. Lectures in mathematical models of turbulence. London, England: Academic Press; 1972.
[43] Yakhot V, Orszag SA. Renormalization group analysis of turbulence I basic theory. J Sci Comput. 1986;1(1):1–51.
[44] Shih TH, Liou WW, Shabbir A, Yang Z, Zhu J. A new-eddy-viscosity model for high reynolds number turbulent flows-model development and validation. Comput Fluids. 1995;24(3):227–38.
[45] Nicoud F, Ducros F. Subgrid-scale stress modelling based on the square of the velocity gradient tensor. Flow Turbulence, Combust. 1999;62(3):183–200.
[46] Pope SB. Turbulent flows. Cambridge: Cambridge University Press; 2000.
[47] Celik IB, Cehreli ZN, Yavuz I. Index of resolution quality for large eddy simulations. J Fluids Eng. 2005;127(5):949–58.
[48] Santos EG, Shi J, Gavaises M. Investigation of cavitation and air entrainment during pilot injection in real size multi-hole diesel nozzles. Fuel. 2020;263:116746.
[49] Battistoni M, Xue QL, Som S. Large-Eddy simulation (LES) of spray transients: start and end of injection phenomena. Oil Gas Sci Technol–Revue d'IFP Energ nouvelles. 2016;71(1):4.
[50] Kahila H, Kaario O, Ahmad Z, Ghaderi Masouleh M, Tekgül B, Larmi M, et al. A large-eddy simulation study on the influence of diesel pilot spray quantity on methane-air flame initiation. Combust Flame. 2019;206:506–21.
[51] Hu Z, Shi Y, Mo X, Xu J, Zhao B, Lin Y, et al. Research progress of large eddy simulation in internal combustion engine. Chin J Theor Appl Mech. 2013;45(04):467–82.
[52] Ghiji M, Goldsworthy L, Brandner PA, Soteriou C, Bauer W. Numerical and experimental investigation of early stage diesel sprays. Fuel. 2016;175:274–86.
[53] Wang ZM, Ding H, Ma X, Xu H, Wyszynski ML. Ultra-high speed imaging study of the diesel spray close to the injector tip at the initial opening stage with single injection. Appl Energy. 2016;165:335–44.
[54] Wang Z, Li Y, Wang C, Xu H, Wyszynski ML. Experimental study on primary breakup of diesel spray under cold start conditions. Fuel. 2016;183:617–26.
[55] Payri R, Garcia JM, Salvador FJ. Using spray momentum flux measurements to understand the influence of diesel nozzle geometry on spray characteristics. Fuel. 2005;84(5):551–61.
[56] Siebers DL. Liquid-phase fuel penetration in diesel sprays. SAE technical paper 980809; 1998.
[57] Som S, Aggarwal SK. Effects of primary breakup modeling on spray and combustion characteristics of compression ignition engines. Combust Flame. 2010;157(6):1179–93.
[58] Li Y, Ries F, Nishad K, Sadiki A. Impact of atomization process on the morphology of a gasoline direct injection jet (ECN Spray G2) using large Eddy simulation including in-nozzle flow and phase change. In Proceedings of ILASS-Asia 2020. Zhenjiang, China; 2020.